Supporting Information for: Thermal Conductivity Enhancement in Ion-Irradiated Hydrogenated Amorphous Carbon Films

Ethan A. Scott,[†] Sean W. King,[‡] Nanette N. Jarenwattananon,[¶] William A. Lanford,[§] Han Li,[‖] James Rhodes,[‡] and Patrick E. Hopkins[*,†,⊥,#]

[†]*Department of Mechanical and Aerospace Engineering, University of Virginia, Charlottesville, Virginia 22904, United States*

[‡]*Logic Technology Development, Intel Corporation, Hillsboro, Oregon 97124, United States*

[¶]*Center for Materials Characterization in Oregon, University of Oregon, Eugene, OR 97403, United States*

[§]*Physics Department, University at Albany, SUNY, Albany, NY 12222, United States*

[‖]*CQN Labs, Intel Corporation, Hillsboro, Oregon 97124, United States*

[⊥]*Department of Materials Science and Engineering, University of Virginia, Charlottesville, Virginia 22904, United States*

[#]*Department of Physics, University of Virginia, Charlottesville, Virginia 22904, United States*

E-mail: phopkins@virginia.edu

Contents

S1 Details on Film Deposition

The a-C:H films for this study were prepared via plasma-enhanced chemical vapor deposition (PECVD) onto Si (001) substrates, 300 mm in diameter, using a commercially available dual radio frequency system.[1] The films were grown to a nominal thickness of 200 nm, which was later verified with spectroscopic ellipsometry. Three groups of films (labeled Films 1 - 3) were produced with varying levels of hydrogen prior to implantation. The atomic composition for each as-deposited film was verified via combined Rutherford backscattering spectroscopy (RBS) and nuclear reaction analysis (NRA) measurements.[2] In addition, the sp^2/sp^3 ratio for the as-deposited films was analyzed via nuclear magnetic resonance analysis (NMR). Preparation of the material for NMR analysis required powderization of the films, which was performed for Films 2 and 3, but could not be performed for Film 1. A similar value for Film 1 may be expected given the similarity between Films 2 and 3 (1.9 and 2.1, respectively).

S2 Details on Thermal Measurements

S2.1 Thermal Model Parameters

To measure the thermal conductivity of the a-C:H films, the ratio of the reflected TDTR probe signal was recorded with a lock-in amplifier and analyzed as a function of pump-probe delay time. The data were fitted with a multilayer heat diffusion model,[3] in which the thermal conductivity of the a-C:H film was treated as a fitting parameter. Example fit parameters (thermal conductivity (κ), thickness (d), and volumetric heat capacity (C)) used in the thermal model are shown in Table S1. We observe negligible sensitivity to the thermal boundary conductances (G) within the system, and thus are not included in the table.

Table S1: Table of representative values used in the thermal model.

Layer	Material	κ (W m^{-1} K^{-1})	d (nm)	C (MJ m^{-3} K^{-1})
1	Al	100	80	2.43
2	a-C:H	0.53	$\sim$200	$\sim$1.69
3	Si	123	semi-inf	1.65

For layer 1, we apply a value of 100 W m^{-1} K^{-1} for the thermal conductivity of the aluminum films, determined from four-point probe measurement and application of the Wiedemann-Franz law. We determine the thickness from picosecond acoustic measurements,[4] and assume a literature value of 2.43 MJ m^{-3} K^{-1} for the volumetric heat capacity.[5] We treat the thermal boundary conductance across the Al/a-C:H interface as an open fitting parameter, but find there is negligible sensitivity (see Fig. S2). For layer 2, thermal conductivity is treated as a fitting parameter and the volumetric heat capacity is calculated from a modified Kopp's rule,[6–8] based upon the atomic concentration and densities of the films, resulting in values ranging from 1.61 to 1.77 MJ m^{-3} K^{-1}. There is no sensitivity to the interface of the a-C:H film and the Si substrate, as as such we consider it as infinite. For the silicon substrate, we apply a value of 123 W m^{-1} K^{-1}, determined from a sample with no a-C:H deposited, and assume a literature value of 1.65 MJ m^{-3} K^{-1} for the volumetric heat capacity.[9] An example of a model fit is displayed in Fig. S1 for Film 2 before and after

implantation.

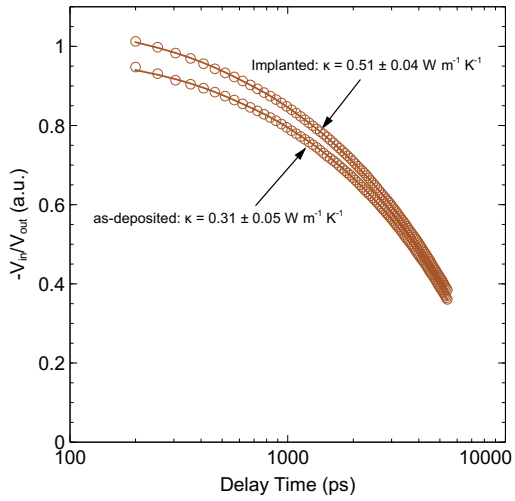

Figure S1: Representative TDTR data (open circles) and corresponding model fit (solid line) for an as-deposited vs implanted film. In this case, the films are as-deposited and irradiated examples of Film 2.

S2.2 Parameter Sensitivity

In consideration of the sensitivity of the thermal model (S) to a given parameter (x), we perform a sensitivity analysis in a similar manner as Gundrum *et al.*[10] In general, a higher absolute value of S_x indicates a higher sensitivity to parameter, x. We provide an example sensitivity analysis using representative data tabulated in Table S2. From the calculation, highest sensitivity is observed for C_1, C_2, d_1, and κ_2. There is lesser sensitivity to d_2, and negligible sensitivity for the remaining parameters. As mentioned above, regarding those parameters for which there is appreciable sensitivity, C_1 is assumed from literature, d_1 is determined through picosecond acoustic analysis, C_2 is calculated based upon measured atomic composition and density, d_2 is measured with spectroscopic ellipsometry, and κ_2 is determined through least squares minimization of the difference between the thermal model and measured TDTR data.

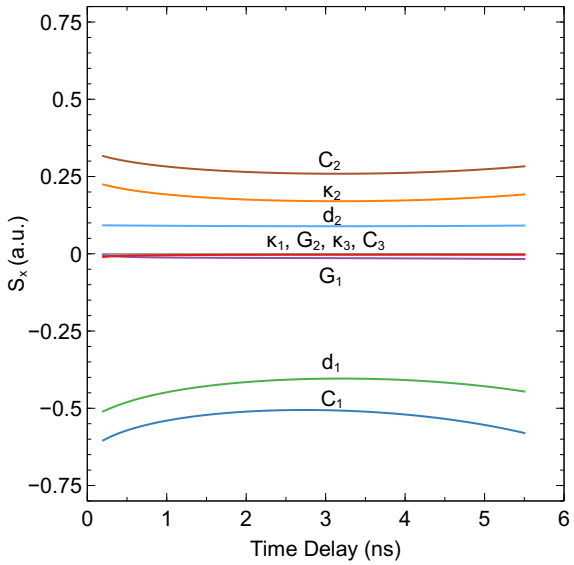

Figure S2: Representative sensitivity analysis of material parameters in the thermal model. For this calculation, model parameters from Table S2 are applied.

Table S2: Values used for the sensitivity analysis calculations displayed in Fig. S2

Layer	Material	κ (W m^{-1} K^{-1})	d (nm)	C (MJ m^{-3} K^{-1})	G (MW m^{-2} K^{-1})
1	Al	100	80	2.43	150
2	a-C:H	0.53	200	1.69	150
3	Si	123	semi-inf.	1.65	n/a

S2.3 Thermal Penetration Depth

We consider the 1/e thermal penetration depth, δ, from TDTR measurement, to be calculated as:[11]

$$\delta = \sqrt{\kappa/(\pi C f)}, \tag{S1}$$

where κ is the thermal conductivity of the material, C is the volumetric heat capacity, and f is the modulation frequency of the pump. For this calculation, we apply an average volumetric heat capacity (1.69 MJ m^{-3} K^{-1}), and a modulation frequency of 8.8 MHz. We plot δ as a function of the thermal conductivity in Figure S3(a). As the thermal penetration depth increases as a function of thermal conductivity, we consider the high-thermal conductivity case; the most thermally conductive of all the samples in the study has a thermal conductivity of 0.8 W m^{-1} K^{-1}. This corresponds to a thermal penetration depth of approximately 131 nm. For that particular sample, the thickness is 172 nm. The thinnest of all samples is 161 nm, and therefore the thermal penetration depth never extends beyond the thickness of the a-C:H layer.

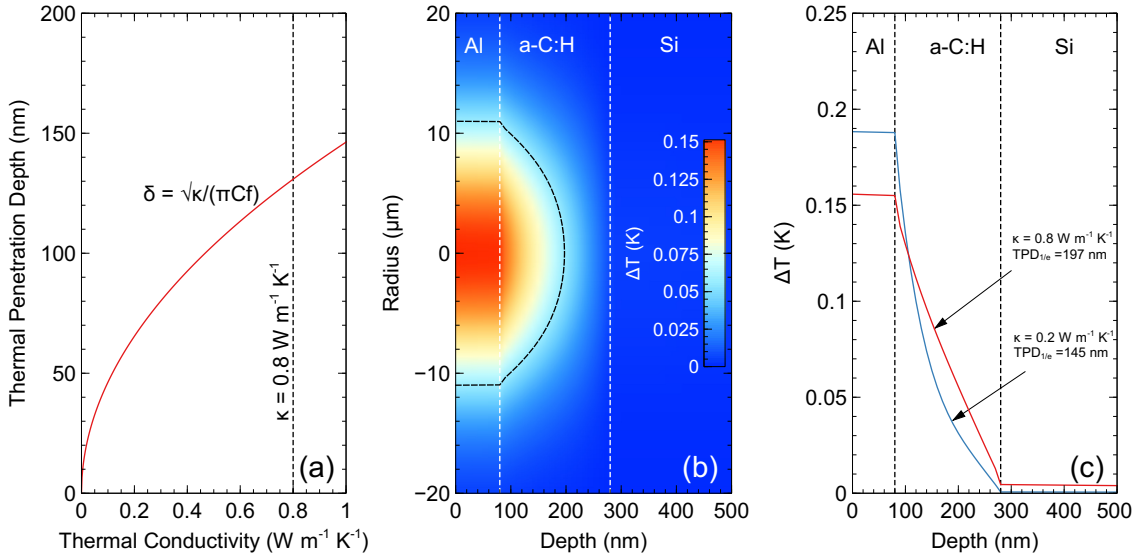

Figure S3: (a) Thermal penetration depth calculated according to Eqn. S1. (b) Representative two-dimensional temperature profile of the heating induced in an a-C:H sample from TDTR measurement. The temperature profiles at the center of the laser spot is shown in (c) for a film with a thermal conductivity of 0.8 W m^{-1} K^{-1} (red) and 0.2 W m^{-1} K^{-1} (blue).

Furthermore, we note that Eqn. S1, is an analytical estimation of the thermal penetration depth, which tends toward overestimation, as it does not take into account thermal spreading within the

aluminum transducer, nor the temperature drop at the aluminum/film interface.[12] For a more accurate assessment of the thermal penetration depth in the samples, we perform detailed calculations of the depth-dependent temperature rise from a multilayer heat diffusion calculation[12,13] (for a film with thermal conductivity of 0.8 W m^{-1} K^{-1}) and find the 1/e thermal penetration depth to be 197 nm from the surface (Figure S3(a,b)). Given that the aluminum transducer is 80 nm, this corresponds to a depth of 117 nm within the a-C:H film. This depth is further reduced for films of lower thermal conductivity. Taken together, these results demonstrate that the penetration depth is never great enough to penetrate the beyond film, and therefore we do not expect reductions in the film thickness to alter the sensitivity of the measurement.

S2.4 Thermal Resistance

The ability to resolve the thermal conductivity of a layer or the thermal boundary conductance of an interface is often dictated by its relative thermal resistance. We consider the thermal resistance of the interface, calculated as $R_{interface} = 1/G_{Al/a-C:H}$, and the thermal resistance of the film, calculated as $R_{film} = d_{film}/\kappa_{film}$. We consider two extremes of thermal conductivity, κ = 0.2 and 0.8 W m^{-1} K^{-1}, which correspond to the most and least thermally resistive films measured, respectively. While we are unable to directly fit for the thermal boundary conductance, we consider values ranging from 100 - 250 MW m^{-2} K^{-1}, which spans a range representative of Al/dielectric interfaces.[14] In Fig. S2, we plot the thermal resistance of the films (solid lines), the range of interface resistances (grey region), and the combined interface and film resistances (colored regions). In the limit of thin film thickness (less than 10 nm), the interface serves as the dominant source of thermal resistance. However as the film thickness increases, the dominant thermal resistance source transitions to that of the film. At the nominal film thickness of 200 nm (black dashed line), the thermal resistance of the film is much greater than of the interface, regardless of the film thermal conductivity.

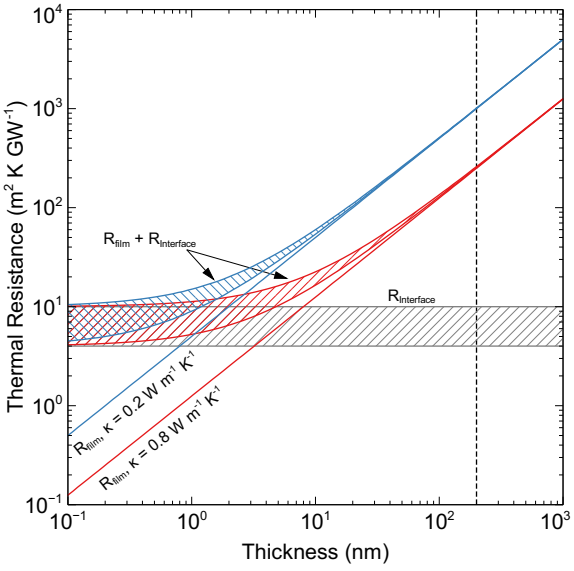

Figure S4: Thermal resistance of the films (solid lines), and total thermal resistance attributed to the film and interface resistance between the Al transducer and film surface. The calculations consider two extremes of film thermal conductivity, $\kappa = 0.2$ W m^{-1} K^{-1} (blue) and $\kappa = 0.8$ W m^{-1} K^{-1} (red). Furthermore we consider interface resistance for values spanning 4 - 10 m^2 K GW^{-1}, which spans a range representative of aluminum/dielectric interfaces.[14,15]

S3 NMR Measurements

Solid-state NMR spectra were collected using a 11.74 T magnet with a Varian VNMRS spectrometer operating at 500.23 MHz for ^{1}H and 125.73 MHz for ^{13}C. Experiments were performed on a Phoenix 1.6-mm triple resonance MAS probe operating in ^{1}H/^{13}C mode. Magic angle spinning (MAS) was used to collect direct polarization NMR spectra at a spinning rate of 20 kHz. ^{13}C chemical shifts were externally referenced to the upfield methane peak of adamantane at 29.46 ppm. ^{13}C direct polarization (DP) NMR experiments were performed with a ^{13}C 90 degree pulse length of 2 us, a relaxation delay of 15 s, and 60kHz two-pulse phase modulated (TPPM) ^{1}H decoupling during signal acquisition. ^{13}C cross polarization (CP) NMR experiments under the Hartmann-Hahn matching condition were performed with a ^{1}H 90 degree pulse length of 2 us, varying contact times between 0.5 to 5 ms, a relaxation delay of 3 s, and 60kHz TPPM ^{1}H decoupling during signal acquisition.

While CP NMR provides qualitative information about the type of carbon bonds present, the DP experiments provide quantitative information. In this case, $sp^2 : sp^3$ carbon hybridization ratios were determined by integrating resonances associated with a specific chemical shift range. Spectra from Film 2 and 3 are displayed in Fig. S5(a) and (b), respectively.

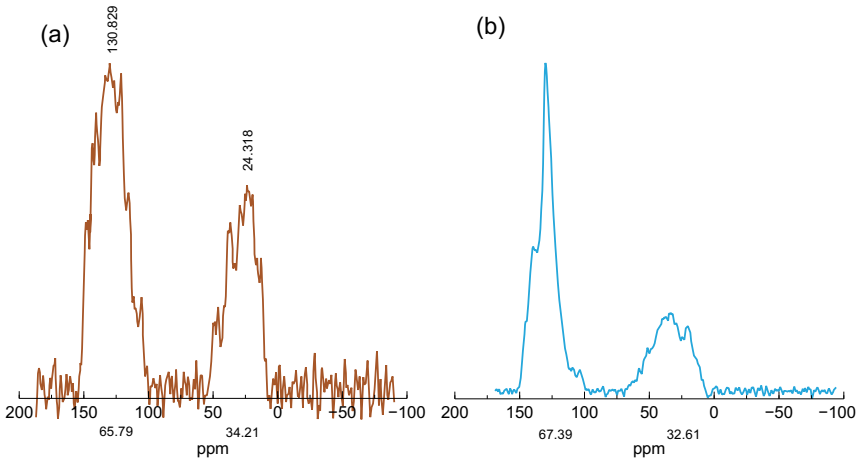

Figure S5: NMR spectra from DP NMR experiments for Films 2 (a) and 3 (b). The resonances at approximately 130.8 and 24.3 ppm are related to sp^2 and sp^3 orbitals, respectively. The integrated areas for each resonance, shown below the axis, are used to calculate the $sp^2 : sp^3$ carbon hybridization ratio.

S4 FTIR Measurements

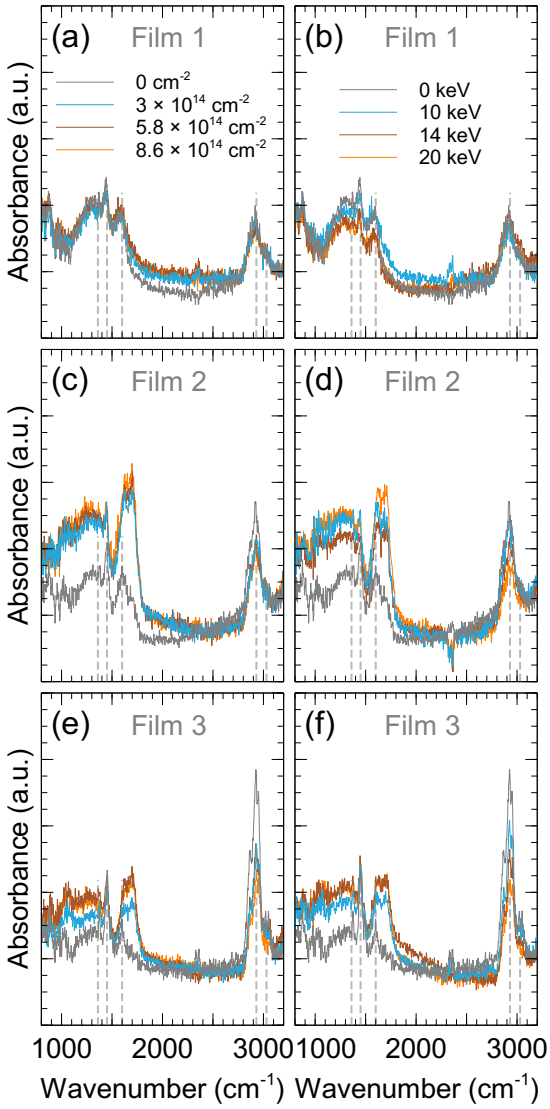

Figure S6: FTIR spectra for all films collected over a range of 800 cm^{-1} to 3200 cm^{-1}. (a), (c), and (e) display the spectra for varying ion fluences for Films 1, 2, and 3, respectively. (b), (d), and (f) display the spectra for varying ion energies for Films 1, 2, and 3, respectively. The absorbance peaks at 1360, 1450, 1600, 2930, and 3030 cm^{-1} represent sp^3 CH_3 bending, sp^2 CH_2 bending, sp^2 C=C stretching, sp^3 C-H stretching, and sp^2 C-H stretching vibrations, respectively.

S5 Film Stress

Beyond increasing stiffness, ion implantation is often utilized in the fabrication of a-C:H films to reduce stress which can lead to wrinkling or delamination of the film.[16] The measured film stress is displayed as a function of ion fluence and energy in Fig. S7(a) and (b), respectively. For Films 1 and 2, the implant produces a reduction in the compressive stress, which is more pronounced in Film 1. For Film 3, the stress state transitions from slightly tensile to slightly compressive.

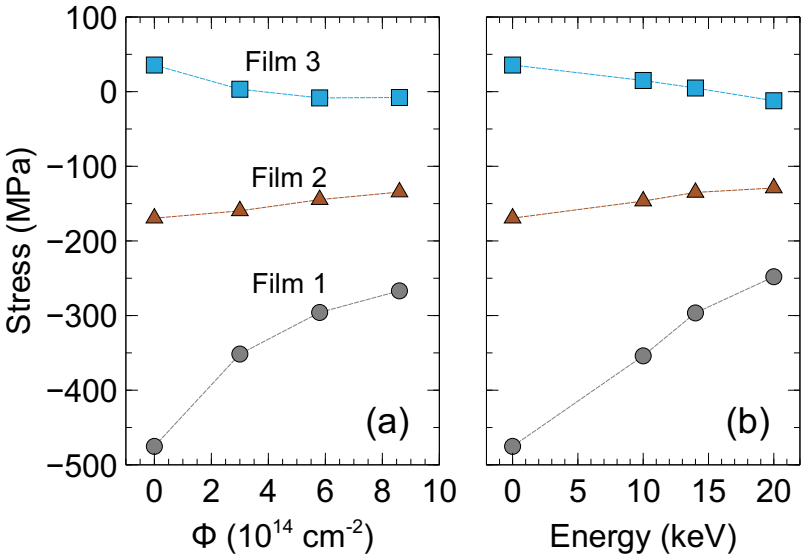

Figure S7: Nominal film stress as a function of ion fluence (a) and energy (b).

S6 Amorphous limit model

The thermal conductivity is discussed in the framework of the "amorphous limit" model based upon the work of Cahill, Watson, and Pohl.[17] In this model, thermal transport is considered as being limited to a random walk of atomic vibrations with a limited length scale of energy exchange on the order of half a period of oscillation.[18] As the nominal accuracy of this model is variable depending upon material system,[18–20] we focus upon the trends in relation to the experimental data. With this model, the thermal conductivity can be expressed as

$$\kappa_{min} = \left(\frac{\pi}{6}\right)^{\frac{1}{3}} k_B n_A^{\frac{2}{3}} \sum_{i=1}^{3} v_i \left(\frac{T}{\Theta_i}\right)^2 \int_0^{\frac{\Theta_i}{T}} \frac{x^3 e^x}{(e^x-1)^2} dx, \tag{S2}$$

where k_B is the Boltzmann constant, n_A is the atomic number density, calculated from[21] $n_A = N_A\rho/M$ (N_A is Avogadro's number, and M is atomic mass), i is an index for the phonon polarization, v is the sound speed, T is temperature, and Θ is the cutoff temperature, calculated for for each polarization as $\Theta_i = v_i(\hbar/k_B)(6\pi^2 n_A)^{1/3}$ (Refs. 22,23), where $\hbar$ is the reduced Planck constant. For the atomic mass, we apply a rule of mixtures calculation weighting the C, N, O, and H concentration for each film, measured via NRA. The sound speed for each polarization is calculated from a continuum mechanics approach using measurements of the film density and elastic modulus, which has been demonstrated as an accurate approximation in other hydrogenated amorphous films.[18] With this approach, the longitudinal sound speed can be expressed as $v_L = \sqrt{E(1-\nu)/(\rho(1+\nu)(1-2\nu))}$ and $v_T = \sqrt{E/(2\rho(1+\nu))}$, where ν is Poisson's ratio.[18] For ν we apply a value of 0.3.[21,22,24]

Calculation of the thermal conductivity as a function of a single parameter is complicated by correlation between parameters (namely, ρ, E, and %H, in this case). For example, if the hydrogen content is reduced, the density and elastic modulus correspondingly increase. For simplicity, we assume linear relationships between the parameters based upon experimental measurements tabulated in Table S3.

Table S3: Nominal values of hydrogen content, density, and modulus of elasticity used for calculation of κ_{min}. As these values are correlated, we assume linear relationships between parameters over the given ranges in the model. For example, in when calculating κ_{min} as a function of %H, we considered E and ρ to vary linearly with %H over the given range of %H.

	%H (%)	ρ (g cm^{-3})	E (GPa)
Film 1			
	33.9	1.5	61.8
	33.6	1.6	69.4
	31.1	1.6	69.2
	32.3	1.7	72.2
	30.8	1.6	61.9
	31.5	1.5	64.2
	31.9	1.5	63.8
Film 2			
	36.3	1.5	19.6
	33.4	1.4	21.3
	35.5	1.5	22.5
	41.7	1.4	18.4
	37.7	1.5	18.5
	34.2	1.5	20.8
	35.0	1.6	24.5
Film 3			
	46.5	1.2	6.2
	40.9	1.3	4.3
	41.0	1.4	5.4
	38.0	1.4	6.8
	39.3	1.2	6.2
	39.1	1.2	7.1
	38.1	1.2	9.4

References

(1) Antonelli, G. A.; Reddy, S.; Subramonium, P.; Henri, J.; Sims, J.; O'loughlin, J.; Shamma, N.; Schlosser, D.; Mountsier, T.; Guo, W.; Sawin, H. Patterning with Amorphous Carbon Thin Films. *ECS Trans.* **2011**, *35*, 701–716.

(2) Lanford, W. A. et al. Nuclear reaction analysis for H, Li, Be, B, C, N, O and F with an RBS check. *Nucl. Instrum. Methods Phys. Res., Sect. B* **2016**, *371*, 211–215.

(3) Cahill, D. G. Analysis of heat flow in layered structures for time-domain thermoreflectance. *Rev. Sci. Instrum.* **2004**, *75*, 5119–5122.

(4) Grahn, H. T.; Maris, H. J.; Tauc, J. Picosecond ultrasonics. *IEEE J. Quantum Electron.* **1989**, *25*, 2562–2569.

(5) Scott, E. A.; Smith, S. W.; Henry, M. D.; Rost, C. M.; Giri, A.; Gaskins, J. T.; Fields, S. S.; Jaszewski, S. T.; Ihlefeld, J. F.; Hopkins, P. E. Thermal resistance and heat capacity in hafnium zirconium oxide (Hf1–xZrxO2) dielectrics and ferroelectric thin films. *Appl. Phys. Lett.* **2018**, *113*, 192901.

(6) Hurst, J. E.; Keith Harrison, B. ESTIMATION OF LIQUID AND SOLID HEAT CAPACITIES USING A MODIFIED KOPP'S RULE. *Chem. Eng. Commun.* **1992**, *112*, 21–30.

(7) Harikrishna, H.; Lanford, W. A.; King, S. W.; Huxtable, S. T. Thermal conductivity of plasma deposited amorphous hydrogenated boron and carbon rich thin films. *J. Nucl. Mater.* **2019**, *514*, 154–160.

(8) Harikrishna, H.; Huxtable, S. T.; Shir, I. B.; Kababya, S.; Schmidt, A.; Dutta, D.; Liu, M.; Gidley, D.; Lanford, W. A.; Hellgren, N.; Ege, C.; Mays, E.; Bielefeld, J.; King, S. W. Thermal conductivity-structure-processing relationships for amorphous nano-porous organosilicate thin films. *J. Porous Mater.* **2020**, *27*, 565–586.

(9) Scott, E. A.; Hattar, K.; Rost, C. M.; Gaskins, J. T.; Fazli, M.; Ganski, C.; Li, C.; Bai, T.; Wang, Y.; Esfarjani, K.; Goorsky, M.; Hopkins, P. E. Phonon scattering effects from point and extended defects on thermal conductivity studied via ion irradiation of crystals with self-impurities. *Phys. Rev. Mater.* **2018**, *2*, 095001.

(10) Gundrum, B. C.; Cahill, D. G.; Averback, R. S. Thermal conductance of metal-metal interfaces. *Phys. Rev. B* **2005**, *72*, 245426.

(11) Koh, Y. K.; Singer, S. L.; Kim, W.; Zide, J. M. O.; Lu, H.; Cahill, D. G.; Majumdar, A.; Gossard, A. C. Comparison of the 3ω method and time-domain thermoreflectance for measurements of the cross-plane thermal conductivity of epitaxial semiconductors. *J. Appl. Phys.* **2009**, *105*, 054303.

(12) Braun, J. L.; Hopkins, P. E. Upper limit to the thermal penetration depth during modulated heating of multilayer thin films with pulsed and continuous wave lasers: A numerical study. *J. Appl. Phys.* **2017**, *121*, 175107.

(13) Braun, J. L.; Szwejkowski, C. J.; Giri, A.; Hopkins, P. E. On the Steady-State Temperature Rise During Laser Heating of Multilayer Thin Films in Optical Pump–Probe Techniques. *J. Heat Transfer* **2018**, *140*.

(14) Cheaito, R.; Gaskins, J. T.; Caplan, M. E.; Donovan, B. F.; Foley, B. M.; Giri, A.; Duda, J. C.; Szwejkowski, C. J.; Constantin, C.; Brown-Shaklee, H. J.; Ihlefeld, J. F.; Hopkins, P. E. Thermal boundary conductance accumulation and interfacial phonon transmission: Measurements and theory. *Phys. Rev. B* **2015**, *91*, 035432.

(15) Hopkins, P. E. Thermal Transport across Solid Interfaces with Nanoscale Imperfections: Effects of Roughness, Disorder, Dislocations, and Bonding on Thermal Boundary Conductance. *ISRN Mechanical Engineering* **2013**, *2013*.

(16) Iwamura, E. *Tribology and Interface Engineering Series*; Elsevier: Walthm, MA, USA, 2008; Vol. 55; pp 283–303.

(17) Cahill, D. G.; Watson, S. K.; Pohl, R. O. Lower limit to the thermal conductivity of disordered crystals. *Phys. Rev. B* **1992**, *46*, 6131–6140.

(18) Braun, J. L.; King, S. W.; Giri, A.; Gaskins, J. T.; Sato, M.; Fujiseki, T.; Fujiwara, H.; Hopkins, P. E. Breaking network connectivity leads to ultralow thermal conductivities in fully dense amorphous solids. *Appl. Phys. Lett.* **2016**, *109*, 191905.

(19) Mizuno, H.; Mossa, S.; Barrat, J.-L. Beating the amorphous limit in thermal conductivity by superlattices design. *Sci. Rep.* **2015**, *5*, 1–15.

(20) Cheng, Z.; Weidenbach, A.; Feng, T.; Tellekamp, M. B.; Howard, S.; Wahila, M. J.; Zivasatienraj, B.; Foley, B.; Pantelides, S. T.; Piper, L. F. J.; Doolittle, W.; Graham, S. Diffuson-driven ultralow thermal conductivity in amorphous Nb_2O_5 thin films. *Phys. Rev. Mater.* **2019**, *3*, 025002.

(21) Shamsa, M.; Liu, W. L.; Balandin, A. A.; Casiraghi, C.; Milne, W. I.; Ferrari, A. C. Thermal conductivity of diamond-like carbon films. *Appl. Phys. Lett.* **2006**, *89*, 161921.

(22) Arlein, J. L.; Palaich, S. E. M.; Daly, B. C.; Subramonium, P.; Antonelli, G. A. Optical pump-probe measurements of sound velocity and thermal conductivity of hydrogenated amorphous carbon films. *J. Appl. Phys.* **2008**, *104*, 033508.

(23) Bullen, A. J.; O'Hara, K. E.; Cahill, D. G.; Monteiro, O.; von Keudell, A. Thermal conductivity of amorphous carbon thin films. *J. Appl. Phys.* **2000**, *88*, 6317–6320.

(24) Ferrari, A. C.; Robertson, J.; Beghi, M. G.; Bottani, C. E.; Ferulano, R.; Pastorelli, R. Elastic constants of tetrahedral amorphous carbon films by surface Brillouin scattering. *Appl. Phys. Lett.* **1999**, *75*, 1893–1895.